

Regularisation of the Ostwald supersaturation model for Liesegang bands

J. M. Duley¹, A. C. Fowler^{1,2}, I. R. Moyles³, and S. B. G. O’Brien¹

¹MACSI, University of Limerick, Limerick, Ireland

²OCIAM, University of Oxford, Oxford, UK

³Department of Mathematics and Statistics, York University, Canada

June 15, 2019

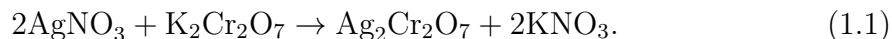
Abstract

In a previous paper, we analysed the Keller–Rubinow formulation of Ostwald’s supersaturation theory for the formation of Liesegang rings or Liesegang bands, and found that the model is ill-posed, in the sense that after the termination of the first crystal front growth, secondary bands form, as in the experiment, but these are numerically found to be a single grid space wide, and thus an artifact of the numerical method. This ill-posedness is due to the discontinuity in the crystal growth rate, which itself reflects the supersaturation threshold inherent in the theory. Here we show that the ill-posedness can be resolved by the inclusion of a relaxation mechanism describing an impurity coverage fraction, which physically enables the transition in heterogeneous nucleation from precipitate-free impurity to precipitate-covered impurity.

Keywords: Liesegang rings, Keller–Rubinow model, Ostwald supersaturation theory.

1 Introduction

Liesegang rings are bands of precipitate which are formed in a number of reactions, of which the classic one studied by Liesegang (1896) involved silver nitrate and potassium dichromate. Rings are formed when the experiment is done in a petri dish, whereas bands are formed (as in figure 1) when it is done in a test tube. This reaction is given by



As shown in figure 1, silver dichromate is precipitated in a series of bands when a gel containing a weak potassium dichromate solution has a thin layer of silver nitrate

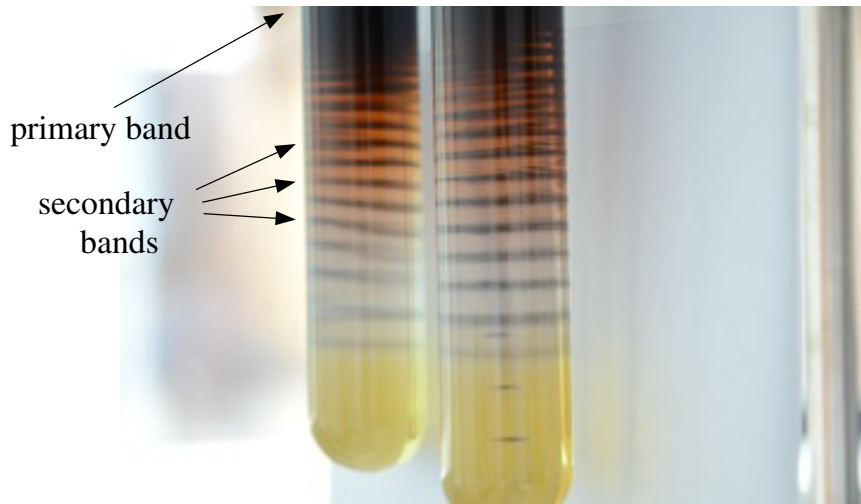


Figure 1: Formation of Liesegang bands in test tubes.

solution placed on top of it. The silver ions diffuse through the gel, reacting with the dichromate, and forming first an initial precipitate whose growth terminates, following which a series of bands are formed. If x_n denotes the distance of the n -th band below the first crystal front, then two ‘laws’ of note are the time law (Morse and Pierce 1903), which states that $x_n \propto \sqrt{t}$, and the space law, which states that x_{n+1}/x_n is a constant (Jablczynski 1923), normally greater than one.

Immediately following Liesegang’s announcement, Ostwald (1897a,b) proposed that the bands could be explained by the supersaturation necessary to form the precipitate, and a number of subsequent studies have developed the resulting theory (Prager 1956, Wagner 1950, Stern 1954, Zel’dovich *et al.* 1962, Keller and Rubinow 1981, Smith 1984).

However, while this theory retains its popularity, it is not the only one; a variant is the post-nucleation theory (Feeney *et al.* 1983, Flicker and Ross 1974, Venzl 1986, Kai *et al.* 1982, Venzl and Ross 1982a,b, Lexa and Holba 1993, Müller and Ross 2003), which assumes uniform nucleation and subsequent Ostwald ripening. This theory is particularly relevant in the absence of strong reactant gradients, and has been commonly studied using Cahn–Hilliard theory (Cahn and Hilliard 1958, Falkowitz and Keller 1988, Rácz 1999, Zegeling *et al.* 2011). A variety of other theories and experimental results have been proposed (Polezhaev and Müller 1994, George and Varghese 2005, Skorobogatov and Kamenskii 2006, Lagzi and Ueyama 2009, Smoukov *et al.* 2011), and a useful book describing the phenomenon is that by Henisch (1988).

In the present paper, we will focus on the supersaturation theory, which is most probably relevant in the experimental conditions of figure 1, where there are large gradients of silver nitrate. A mathematical model of this theory was put forward by Keller and Rubinow (1981). In it they describe the reaction and precipitation by the scheme



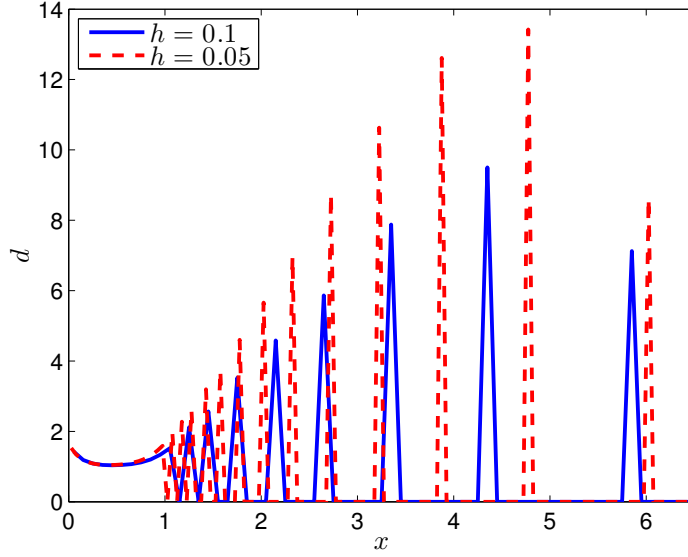


Figure 2: Precipitate d in the numerical solution to the dimensionless Keller–Rubinow model given by equations (10)–(13) in the electronic supplementary material (ESM) for two step sizes on a grid $[0, 10]$ at $t = 60$. The parameter values used (see ESM) are $\delta = 0.05$, $\alpha = 0.25$, $\lambda = 5$, $\nu = 0.1$. Refining the step size increases the number of spikes produced and their locations.

in which A denotes Ag^+ , B denotes $\text{Cr}_2\text{O}_7^{2-}$, C denotes $\text{Ag}_2\text{Cr}_2\text{O}_7^{\text{L}}$ (i. e., dissolved), and D denotes $\text{Ag}_2\text{Cr}_2\text{O}_7^{\text{S}}$ (i. e., precipitated). Here k_{\pm} are normal rate constants, and the precipitation rate p describes supersaturated precipitation and growth. Specifically, crystal nucleation occurs if the concentration c of C (i. e., $\text{Ag}_2\text{Cr}_2\text{O}_7^{\text{L}}$) is greater than a nucleation threshold value c_n which is greater than the saturation concentration c_s , but crystal growth can then continue as long as $c > c_s$. In general dissolution would then occur for $c < c_s$, but this is not allowed in the Keller–Rubinow model, and is in any case irrelevant to the experimental system. The precipitation rate p is given by

$$p = \begin{cases} q[c - c_s]_+ & \text{if } c \geq c_n > c_s \text{ or } d > 0, \\ 0 & \text{if } c < c_n \text{ and } d = 0, \end{cases} \quad (1.3)$$

where $[y]_+ = \max(y, 0)$ and q is a constant: d is the concentration of D; the concentrations are measured in moles l^{-1} (M).

The mathematical detail of the Keller–Rubinow model was described by Duley *et al.* (2017) and is included again in the electronic supplementary material (ESM). A numerical solution of the model is shown in figure 2. A primary band is followed by a sequence of secondary bands, but these are only one grid point wide, and the numerical solution is grid size dependent.

Numerical computations of supersaturation-type models have been presented by a number of authors (e. g., Büki *et al.* 1995, Fiałkowski *et al.* 2005, Hilhorst *et al.* 2009, Lagzi 2003), but little comment has been offered on the validity of the numerical

results. This, of course, depends on the precise form of model which is used to describe the reaction kinetics, but at least in the Keller–Rubinow model, it is found that following the growth and termination of the first band, a series of unresolved spikes of precipitation occur, as shown in figure 2. Duley *et al.* (2017) show that these spikes indicate an ill-posedness in the model, and that they occur because of the discontinuity in the precipitation rate p given in (1.3). They also suggest that the well-posedness can be restored by proposing an evolution equation for a suitable switching variable, which can enable the transition between the discontinuous states. It is the purpose of the present paper to validate this assertion.

To be more specific, we will elaborate the Keller–Rubinow model by allowing for a description of heterogeneous nucleation in which impurities in the gel become covered gradually. Nucleation occurs when the rate of attachment of precipitate molecules to an impurity surface becomes greater than the rate of detachment, and this causes a layer of precipitate to cover the impurity surface (Dowty 1980). The adjustment is not instantaneous, as it occurs through the accumulation of individual molecules on the surface. Ideally, a description of the process would be stochastic (Becker and Döring 1935, Avrami 1939, Lifshitz and Slyozov 1961, Ben-Naim and Krapivsky 1996, Aldous 1999), but such a derivation is reserved for future work; in the following section, we describe a heuristic model which is consistent with the kinetics of supersaturated nucleation.

2 The enhanced Keller–Rubinow model

2.1 The switching equation

We examine the discontinuity in the Keller–Rubinow growth rate in more detail. The transition occurs when a pristine impurity surface first becomes covered by precipitate. Of course, this does not actually happen instantly. Let f be the fractional area coverage of an impurity surface with precipitate. It seems reasonable then to generalise the growth rate in (1.3) as

$$p = fq[c - c_s]_+, \quad (2.1)$$

where evidently we should have $f = 0$ if $d = 0$, but $f \rightarrow 1$ rapidly if $c > c_n$. We wish to pose a heuristic model which mimics this behaviour, somewhat similarly to the threshold model for river channel formation used by Willgoose *et al.* (1991) (cf. Fowler 1997, p. 270). Because the Keller–Rubinow model does not allow dissolution, it is relatively simple to do this. A straightforward idea is to take

$$t_n f_t = G(f, c) \equiv 2(f - f_1)(f - f_2)(f_3 - f), \quad (2.2)$$

where t_n is an appropriate nucleation time scale and, for example,

$$f_1 = - \left[\frac{c - c_n}{c_n - c_s} \right]_+^2, \quad f_2 = \frac{c_n - c}{c_n - c_s}, \quad f_3 = 1 + \left[\frac{c_s - c}{c_n - c_s} \right]_+^2. \quad (2.3)$$

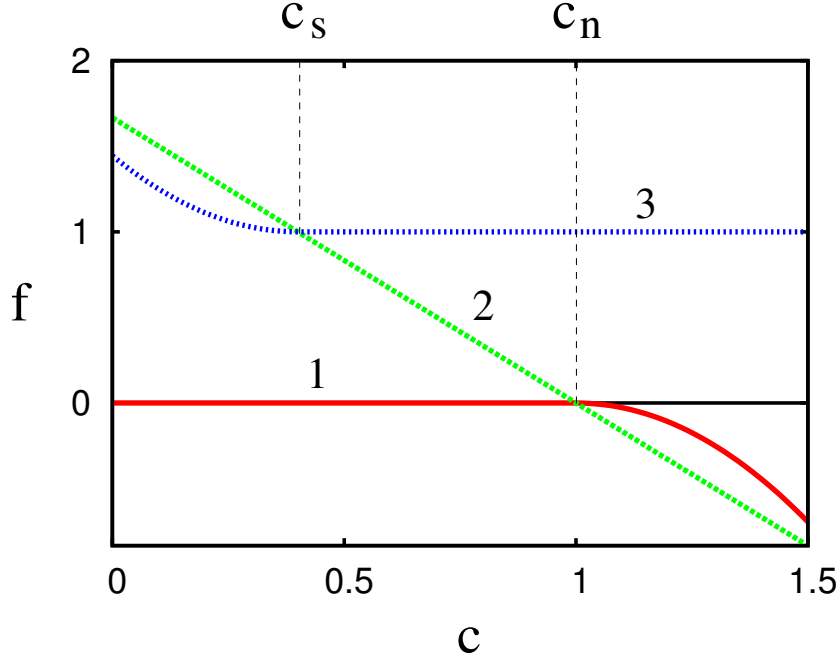


Figure 3: The roots of the cubic $G(f, c)$ as given in (2.3) or (2.6).

Figure 3 illustrates the variation of the roots with c . Since in the evolution of (2.2), the upper and lower roots are stable, while the middle one is unstable, we see that (since also $0 \leq f \leq 1$), this choice forces f to relax to 0 if $c < c_s$, to relax to 1 if $c > c_n$, and to remain at 0 or 1 if $c_s < c < c_n$, depending on prior history (i.e., it remains at 1 if previously $c > c_n$, thus $d > 0$, and it remains at $f = 0$ if $d = 0$). While the prescription of G in (2.2) and (2.3) is suitable for the experimental system under study, it does not properly describe the behaviour in the following circumstance. If c rises above c_n so that $f \rightarrow 1$ and then falls below c_s so that crystal growth ceases, (2.2) implies $f \rightarrow 0$, which is incorrect (once impurities are covered with precipitate they must remain so until the precipitate is dissolved away). So long as c then remains below c_s , as is the case here, it is of no consequence since the growth rate remains zero, but (2.2) as it stands would not allow a correct description of dissolution, were it permitted in the model. The relaxation time t_n of f is supposed small compared to the longer (diffusive) time scales discussed below. The adoption of (2.1) together with (2.2) gives a continuous description of precipitation which reduces to the discontinuous Keller–Rubinow model when $t_n \rightarrow 0$.

We might modify (2.2) by adding a diffusion term. How could f diffuse? It is not that we suppose that the impurities themselves do so, but that if we imagine two impurities close together with different levels of precipitate coverage, then, other things being equal, f will increase more rapidly on the less covered particle, simply as it has more exposed area. This is essentially the same process as Ostwald ripening, and can be represented as a diffusive flux of f down gradients of f , i.e., a diffusion process. The idea of adding a diffusive term is motivated by the expectation that the front where f jumps from 0 to 1 is a travelling wave, for which a simple explanation

is afforded by a reaction-diffusion model. In fact, diffusion is not necessary, and we will persevere with (2.2).

If we non-dimensionalise (2.2) as in equation (5) of ESM (see also Duley *et al.* (2017)), we obtain

$$\kappa f_t = G(f, c), \quad (2.4)$$

where

$$\kappa = \frac{qc_n t_n}{b_0}, \quad (2.5)$$

with, from (2.3),

$$G(f, c) = 2(f - f_1)(f - f_2)(f_3 - f),$$

$$f_1 = -\left[\frac{c-1}{1-\alpha}\right]_+^2, \quad f_2 = \frac{1-c}{1-\alpha}, \quad f_3 = 1 + \left[\frac{\alpha-c}{1-\alpha}\right]_+^2 \quad (2.6)$$

and

$$\alpha = \frac{c_s}{c_n} < 1. \quad (2.7)$$

The dimensionless crystal growth rate is now

$$p = f[c - \alpha]_+, \quad c = AB, \quad (2.8)$$

and is no longer discontinuous. The modified Keller–Rubinow model now takes the form of equations (10) of ESM and (2.4), with G given by (2.6), p given by (2.8), A given by equation (12) of ESM, and the initial and boundary conditions are given by equation (13) of ESM. These are summarised below.

2.2 Analysis of the front

We begin by recollecting the analysis of the first front by Duley *et al.* (2017). First, we gather the equations together:

$$\begin{aligned} B_t &= \delta B_{xx} - f[c - \alpha]_+, \\ \kappa f_t &= G(f, c), \\ c = AB, \quad A &= \frac{\lambda \operatorname{erfc}^2 \theta}{1 + \lambda \nu \operatorname{erfc}^2 \theta}, \quad \theta = \frac{x}{2\sqrt{t}}. \end{aligned} \quad (2.9)$$

The first front propagates as shown in figure 4. Specifically, we define the front to be where f jumps to 1. Actually, it is clear in figure 4 that there is a gap between the front, where f jumps to 1, and the *front tip*, which is the point where $c = 1$ and f commences growing. We denote the front location by $x = s_f$ and the front tip location by $x = s$, and we define

$$s - s_f = \delta X_f, \quad (2.10)$$

and we assume that $X_f \lesssim O(1)$ (in figure 4 $X_f \approx 1.04$). We suppose κ is sufficiently small that we can solve the equation for B with $f = 1$ behind the front and $f = 0$

ahead of it. (We shall see later that this is justified by the fact that the front width (i. e., the width of the region where f jumps from $f \ll 1$ to $f = 1$) is $O(\kappa)$.) Duley *et al.* were able to analyse the front by supposing that δ was small. They then found, by ignoring the diffusive term, that $B = 1$ ahead of the front, while it is an increasing function of x behind the front. The requirement that $c = 1$ at the front tip (and $c < 1$ ahead of it) then dictates the position of the front tip as $x = s = 2\Theta\sqrt{t}$, where $\Theta \approx \Theta_f$ and

$$A(\Theta_f) = 1. \quad (2.11)$$

For the values $\lambda = 5$ and $\nu = 0.1$ which we use in our computations, $\Theta_f \approx 0.509255$.

Also $|A'(\Theta_f)| = 4\sqrt{\frac{\lambda(1-\nu)^3}{\pi}}e^{-\Theta_f^2} = 3.324326$.

This approximate solution has discontinuous slope at the front, and this is smoothed by a weak boundary layer, described by Duley *et al.* in a footnote. For the present purpose, we need to describe this more fully. We put

$$B = 1 + \delta b, \quad x = s + \delta X, \quad s = 2\Theta\sqrt{t}, \quad (2.12)$$

and on solving the leading order forms of the resulting equations (taking $f = 1$ for $X < -X_f$ and $f = 0$ for $X > X_f$) and matching them to the outer solutions, we find, assuming $\dot{s} > 0$,

$$b = \begin{cases} \frac{(1-\alpha)(X+X_f)}{\dot{s}} - \frac{(1-\alpha)}{\dot{s}^2}, & X < -X_f, \\ -\frac{(1-\alpha)}{\dot{s}^2}e^{-\dot{s}(X+X_f)}, & X > -X_f. \end{cases} \quad (2.13)$$

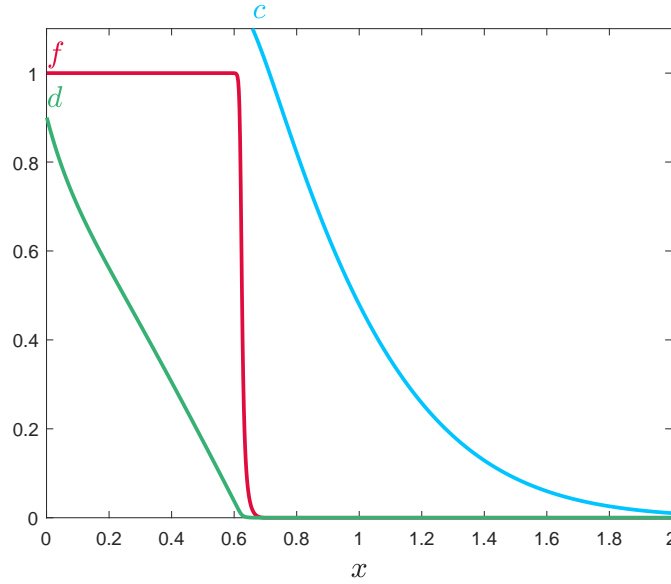


Figure 4: Front propagation at $t = 0.5$. Parameter values are $\lambda = 5$, $\nu = 0.1$, $\alpha = 0.25$, $\delta = 0.05$, $\kappa = 0.01$.

Note for future reference that the equation for f in these coordinates is

$$\kappa \left[f_t - \frac{\dot{s}}{\delta} f_X \right] = G. \quad (2.14)$$

Inserting these expressions into the definition for c , $c = A(\theta)B(x, t)$, defining

$$\Theta = \Theta_f + \delta\Theta_1, \quad (2.15)$$

we find that, correct to $O(\delta)$,

$$c \approx 1 + \delta \left[- \left(\Theta_1 + \frac{X}{2\sqrt{t}} \right) |A'(\Theta_f)| - \frac{(1-\alpha)}{\dot{s}^2} e^{-\dot{s}(X+X_f)} \right] \quad (2.16)$$

in $X > -X_f$, which is the domain of interest for growth of f . Since by definition of the front tip s , $c = 1$ when $X = 0$, we choose

$$\Theta_1 = - \frac{(1-\alpha)e^{-\dot{s}X_f}}{\dot{s}^2 |A'(\Theta_f)|}, \quad (2.17)$$

so that, since also $\dot{s} \approx \Theta_f/\sqrt{t}$,

$$s \approx 2\Theta_f\sqrt{t} - \frac{2\delta(1-\alpha)e^{-\dot{s}X_f}t^{3/2}}{\Theta_f^2 |A'(\Theta_f)|}. \quad (2.18)$$

Using (2.17), we can rewrite (2.16) in the form

$$c \approx 1 + \delta(1-\alpha)e^{-\dot{s}X_f} \left\{ \frac{(t-t_c)X}{\Theta_f\sqrt{t}} + \frac{(1-\dot{s}X - e^{-\dot{s}X})}{\dot{s}^2} \right\}, \quad (2.19)$$

where we use the fact that $\dot{s} \approx \Theta_f/\sqrt{t}$, and

$$t_c = \frac{\Theta_f |A'(\Theta_f)| e^{\dot{s}X_f}}{2(1-\alpha)}. \quad (2.20)$$

If we expand (2.19) for small X and thus X_f (which may be appropriate in the f transition layer), we obtain

$$c \approx 1 + \delta(1-\alpha) \left\{ \frac{X(t-t_c)}{\Theta_f\sqrt{t}} - \frac{1}{2}X^2 \right\}, \quad X > -X_f, \quad (2.21)$$

and now (2.20) gives

$$t_c \approx \frac{\Theta_f |A'(\Theta_f)|}{2(1-\alpha)} \quad (2.22)$$

and (2.18) gives

$$s \approx 2\Theta_f\sqrt{t} - \frac{2\delta(1-\alpha)t^{3/2}}{\Theta_f^2 |A'(\Theta_f)|}. \quad (2.23)$$

The corresponding expression in $X < -X_f$ is similar, but without the quadratic term.

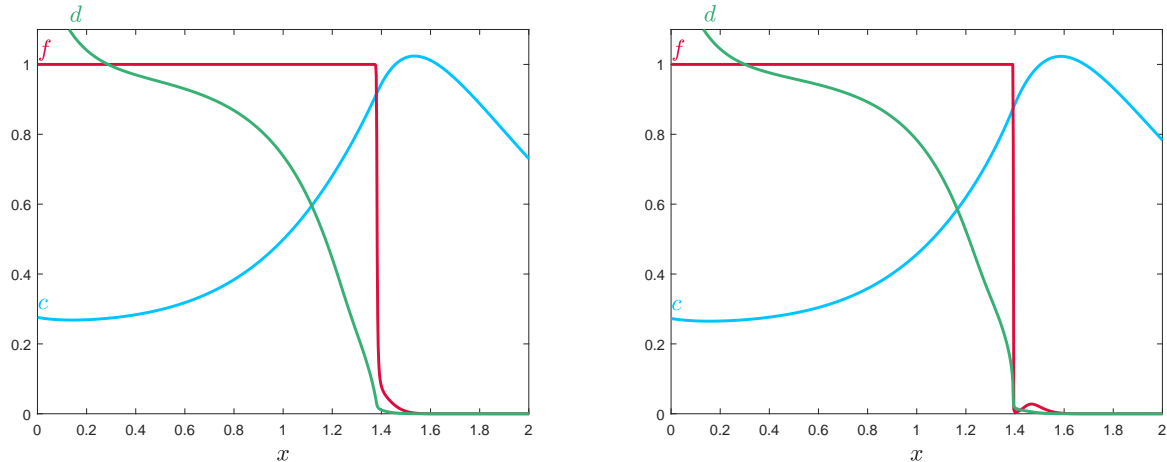


Figure 5: Front propagation at $t = 2.8$ (left) and $t = 3$ (right). Parameter values as in figure 4.

2.3 Transition layer

The reason that the transition front lags behind the position where $c = 1$ is due to the fact that f commences to grow from 0 at $c = 1$, but because the growth is initially very slow, it takes a while for the ‘blow-up’ to occur.

This is more clearly seen in figure 5, as is also the decline in c behind the front due to the continual lowering of B . In fact, we can see from (2.21) that as t increases, c evolves from a decreasing function for $t < t_c$ (figure 4) to a unimodal function with a maximum for $t > t_c$. It is this switch which heralds the cessation of the transition front movement and the formation of secondary bands.

In order to analyse the transition, we need to rescale the variables near the front. The first key thing to realise is that the location of the front tip (where $c = 1$) continues to propagate forward, while $(2.9)_2$, being an ordinary differential equation in time, evolves f at a fixed point in space. Relative to the front tip position, the derivative for f acts as a spatial derivative going backwards; this can be seen in figure 5, for example. When t approaches t_c , then as f evolves backwards in space, c may dip down below 1, causing the small (now positive) root f_2 of G to grow from zero. There is then a competition between the growth of f and the growth (as c decreases with decreasing x) of f_2 ; and if $f < f_2$, its initial growth can not be sustained, and f subsides back to zero. This can be seen in the right hand graph in figure 5. We now analyse this process.

First, we scale the variables in the transition layer by writing

$$\begin{aligned} X &= -\mu\xi, \quad t = t_c + \mu\tau, \\ c &= 1 + \gamma(1 - \alpha)C, \quad f = \gamma\phi, \quad G = \gamma^2g \end{aligned} \tag{2.24}$$

(note that ξ points *backwards* in space), where we anticipate that $\mu, \gamma \ll 1$.

From (2.21), we have

$$\gamma C \approx \delta \mu^2 \left\{ -\frac{\tau \xi}{\Theta_f \sqrt{t_c}} - \frac{1}{2} \xi^2 \right\}. \quad (2.25)$$

Similarly, (2.14) gives

$$\frac{\kappa}{\mu \delta \gamma} (\delta \phi_\tau + \dot{s} \phi_\xi) = g, \quad (2.26)$$

where

$$g = 2 \{ \phi + \gamma [C]_+^2 \} (\phi + C) (1 - \gamma \phi). \quad (2.27)$$

Balance of terms in (2.25) and (2.26) suggests choosing $\gamma = \delta \mu^2$ and $\kappa \dot{s} = \mu \delta \gamma$, whence (since $\dot{s} \approx \Theta_f / \sqrt{t_c}$)

$$\mu = \left(\frac{\kappa \Theta_f}{\delta^2 \sqrt{t_c}} \right)^{1/3}, \quad \gamma = \left(\frac{\kappa^2 \Theta_f^2}{\delta \sqrt{t_c}} \right)^{1/3}, \quad (2.28)$$

and we see that the assumption that $\mu, \gamma \ll 1$ requires $\kappa \ll \delta^2$. At leading order, we thus have

$$\begin{aligned} \frac{\delta \sqrt{t_c}}{\Theta_f} \phi_\tau + \phi_\xi &= g \approx 2(\phi + \gamma [C]_+^2)(\phi + C), \\ C &= -\frac{\tau \xi}{\Theta_f \sqrt{t_c}} - \frac{1}{2} \xi^2. \end{aligned} \quad (2.29)$$

The small term in the definition of g is retained because otherwise ϕ remains at zero; the small τ derivative term for ϕ is retained both because it is easy to manage, and also because it will play a significant rôle in the formation of secondary bands.

Suitable conditions to apply for the solution for ϕ are

$$\phi = 0 \quad \text{at} \quad \xi = 0, \quad \tau = \tau_0, \quad \phi \rightarrow \infty \quad \text{at} \quad \xi = \xi_f(\tau); \quad (2.30)$$

the second condition corresponds to the position of the front, and is commented on further below. We can solve (2.29) using the method of characteristics. Using ξ as the coordinate along the characteristics, these are given by

$$\frac{d\tau}{d\xi} = \frac{\delta \sqrt{t_c}}{\Theta_f}, \quad (2.31)$$

and thus

$$\tau = \tau_0 + \frac{\delta \sqrt{t_c} \xi}{\Theta_f}, \quad (2.32)$$

and the equation to be solved for ϕ along the characteristic is simply

$$\begin{aligned} \frac{d\phi}{d\xi} &\equiv \phi' = g = 2(\phi + \gamma [C]_+^2)(\phi + C), \\ C &= \beta \xi - \frac{1}{2} \Delta \xi^2, \end{aligned} \quad (2.33)$$

where

$$\beta = -\frac{\tau_0}{\Theta_f \sqrt{t_c}}, \quad \Delta = 1 + \frac{2\delta}{\Theta_f^2}. \quad (2.34)$$

The problem of transition thus reduces to the solution of a simple ordinary differential equation. The initial condition at $\xi = 0$ is $\phi = 0$, and as long as $C < 0$ ($c < 1$), ϕ remains zero for $\xi > 0$. Our definition of the front tip means that C increases first to 0 as ξ increases to $\xi = 0$. For $t < t_c$, β is positive, and C increases to zero as ξ increases to zero.

For small $\xi > 0$ with $\beta > 0$, (2.33) implies that

$$\phi \sim \frac{1}{2}\gamma\beta^3\xi^4. \quad (2.35)$$

We see that the small term in γ in (2.33) is essential to initiate growth of ϕ .

Progressing beyond this, we see that ϕ is small for a time, and we write $\phi = \gamma\psi$, and (2.33) is approximately

$$\psi' = 2C(\psi + [C]_+^2), \quad C = \beta\xi - \frac{1}{2}\Delta\xi^2. \quad (2.36)$$

With the initial condition from (2.35), the solution of this is (noting that $[C]_+^2 = C^2$ when $C > 0$, but $[C]_+^2 = 0$ when $C < 0$)

$$\psi = 2e^{H(\xi)} \int_0^{\min(\xi, \xi_0)} \{C(\eta)\}^3 e^{-H(\eta)} d\eta, \quad \xi_0 = \frac{2\beta}{\Delta}, \quad (2.37)$$

where

$$H(\xi) = \beta\xi^2 - \frac{1}{3}\Delta\xi^3. \quad (2.38)$$

We are interested in the condition that allows ψ to become large: but we can see from (2.37) that if $\beta \sim O(1)$, ψ reaches a maximum at $\xi = \xi_0 = 2\beta/\Delta$, and then declines towards zero. In order for ψ to grow, it is necessary (formally) that $\beta \gg 1$. In this case, application of Laplace's method shows that

$$\psi \sim \beta e^{H(\xi)} = \beta e^{\beta\xi^2 - \frac{1}{3}\Delta\xi^3} \quad \text{when} \quad \frac{1}{\sqrt{\beta}} \ll \xi < 2\beta. \quad (2.39)$$

This suggests that there is a critical value of β which distinguishes blow-up from decay, and indeed a graphical analysis of trajectories of (2.33) in the (ξ, ϕ) plane shows that this critical value of β is associated with the unique trajectory for which $\phi \sim -C$ as $\xi \rightarrow \infty$. The approximation (2.39) becomes invalid when $\psi \sim 1/\gamma$, i.e.,

$$\xi \sim \left(\frac{1}{\beta} \ln \frac{1}{\beta\gamma} \right)^{1/2}, \quad (2.40)$$

and

$$\phi \sim \gamma\beta e^H = \gamma\beta e^{\beta\xi^2 - \frac{1}{3}\Delta\xi^3} \quad \text{for} \quad \xi \sim \left(\frac{1}{\beta} \ln \frac{1}{\beta\gamma} \right)^{1/2}. \quad (2.41)$$

Thus we now consider (2.33) when $\phi \sim O(1)$, in which case we have approximately

$$\phi' = 2\phi(\phi + C). \quad (2.42)$$

The solution of (2.42) satisfying (2.41) is

$$\phi = \frac{e^H}{\left[\frac{1}{\gamma\beta} - 2 \int_0^\xi e^{H(\eta)} d\eta \right]}, \quad (2.43)$$

and we thus see that ϕ ultimately blows up (at $\xi = \xi_f$) if the denominator in (2.43) reaches zero there, and this occurs when

$$\int_0^{\xi_f} \exp \left[\beta \xi^2 - \frac{1}{3} \Delta \xi^3 \right] d\xi = \frac{1}{2\gamma\beta}. \quad (2.44)$$

We mentioned earlier the assumption that $\xi = \xi_f$ indeed defines the blow-up location for f as well as ϕ . As $\xi \rightarrow \xi_f$, (2.43) indicates $\phi \sim 1/\{2(\xi_f - \xi)\}$; the relevant re-scaling for the jump to $f = 1$ is thus $\xi = \xi_f + \gamma Z$, and then $f_Z \approx 2f^2(1 - f)$, with approximate solution $2Z = \ln \frac{f}{1-f} - \frac{1}{f}$, so that in terms of x , the front width (where f jumps) is $O(\delta\mu\gamma) = O\left(\frac{\kappa\Theta_f}{t_c^{1/3}}\right)$, and thus always small in practice.

We can use the above results to determine ξ_f . The integral in (2.44) defines a single-valued function

$$\xi_f = F(\beta). \quad (2.45)$$

Since the integrand increases with β and the right hand side decreases, F is a monotonically decreasing function, with $F(\infty) = 0$ and $F(\beta^*) = \infty$, where β^* is defined uniquely by

$$J(\beta^*) \equiv \int_0^\infty \exp \left[\beta^* \xi^2 - \frac{1}{3} \Delta \xi^3 \right] d\xi = \frac{1}{2\gamma\beta^*}. \quad (2.46)$$

Blow-up can not occur for $\beta < \beta^*$. To see this, note that $J(\beta)$ is a monotonically increasing function of β . Then, if $\beta < \beta^*$,

$$\frac{1}{2\gamma\beta} = \int_0^{\xi_f} \exp \left[\beta \xi^2 - \frac{1}{3} \Delta \xi^3 \right] d\xi < J(\beta) < J(\beta^*) = \frac{1}{2\gamma\beta^*} < \frac{1}{2\gamma\beta}, \quad (2.47)$$

which is a contradiction. We must thus have $\beta > \beta^*$ for blow-up to occur.

Returning to the definitions of F and β , we have

$$\begin{aligned} \xi_f(\tau) &= F \left[-\frac{\tau_0}{\Theta_f \sqrt{t_c}} \right], \\ \tau &= \tau_0 + \frac{\delta \sqrt{t_c}}{\Theta_f} \xi_f, \end{aligned} \quad (2.48)$$

and thus

$$\xi_f(\tau) = F \left[\frac{\delta \xi_f}{\Theta_f^2} - \frac{\tau}{\Theta_f \sqrt{t_c}} \right]. \quad (2.49)$$

When $\xi_f \sim O(1)$, we have

$$\xi_f(\tau) \approx F \left[-\frac{\tau}{\Theta_f \sqrt{t_c}} \right], \quad (2.50)$$

as before; but when ξ_f becomes large, (2.49) implies that $\xi_f(\tau)$ is a monotonically increasing function of τ , with

$$\xi_f(-\infty) = 0, \quad \xi_f \sim \frac{\Theta_f \tau}{\delta \sqrt{t_c}} + \frac{\Theta_f^2 \beta^*}{\delta} \quad \text{as } \tau \rightarrow \infty. \quad (2.51)$$

Notice that when this happens,

$$\dot{s}_f = \dot{s} - \delta \frac{d\xi_f}{d\tau} \rightarrow 0, \quad (2.52)$$

thus the first front becomes stationary, as is numerically observed. To leading order, the first front becomes stationary at the value

$$s_f = 2\Theta_f \sqrt{t_c} - \mu \Theta_f^2 \beta^*. \quad (2.53)$$

In more detail, $F(\beta)$ is monotone decreasing from $F(\beta^*) = \infty$ to $F(\infty) = 0$, thus $-\Theta_f^2 F^{-1}(\xi)$ is monotonically increasing with ξ from $-\Theta_f^2 F^{-1}(0) = -\infty$ to $-\Theta_f^2 F^{-1}(\infty) = -\Theta_f^2 \beta^*$, and (with $s \approx 2\Theta_f \sqrt{t}$), we find

$$s_f = 2\Theta_f \sqrt{t_c} - \mu \Theta_f^2 F^{-1}(\xi_f), \quad (2.54)$$

which increases monotonically with time to the limit in (2.53).

The result is more easily understood by consulting the characteristic diagram shown in figure 6. When the parameter τ_0 at $\xi = 0$ is large and negative, then β given by (2.34) is large and positive, and ξ_f is small. As τ increases to $-\tau^* = -\beta^* \Theta_f \sqrt{t_c}$, ξ_f increases towards ∞ . Following this, there is a pause, until a new front tip is formed at $\tau = \tau^*$ and $-\xi = \xi^* = 2\beta^*/\Delta$; this is described in the following section.

2.4 Secondary banding

We have shown that for $t < t_1$, the first front will propagate, but then stop at $x = x_1$. These values are given by

$$t_1 \approx t_c - \mu \Theta_f \sqrt{t_c} \beta^*, \quad x_1 \approx 2\Theta_f \sqrt{t_c} - \mu \Theta_f^2 \beta^*. \quad (2.55)$$

As t increases beyond t_1 , the solution (2.43) still applies for the characteristics emanating from the front tip, but the denominator remains bounded, so that ϕ rises and then decays again, as seen in figure 5 (right). As $\tau_0 \rightarrow 0^-$ ($t \rightarrow t_c^-$), the maximum of ϕ subsides to zero, and for $\tau_0 > 0$ ($\beta < 0$) $C < 0$ for $\xi > 0$ and ϕ remains at zero.

However, when $\beta < 0$, C becomes positive for $\xi < 0$, and the possibility of the formation of a new band arises. Specifically, when $\beta < 0$, we have

$$C = |\beta| \xi_2 - \frac{1}{2} \Delta \xi_2^2, \quad \xi_2 = \xi + \frac{2|\beta|}{\Delta}, \quad (2.56)$$

and we see that a second band will start to grow when $|\beta| > \beta^*$. This occurs at $t = t_2$, where

$$t_2 = t_c + \mu \Theta_f \sqrt{t_c} \beta^*, \quad (2.57)$$

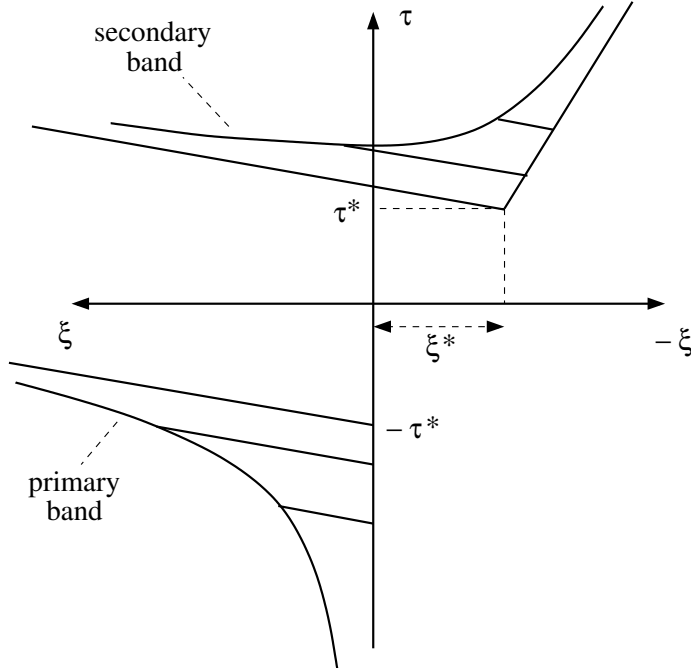


Figure 6: The characteristic (τ, ξ) diagram indicating primary band termination and secondary band formation. Note that ξ increases to the left, in keeping with the direction of increasing x to the right. The mildly slanting lines are the characteristics. The indicated values on the axes are $\tau^* = \beta^* \Theta_f \sqrt{t_c}$, $\xi^* = 2\beta^* / \Delta$. The secondary band in this theory continues to advance towards the top right asymptote, which is $-\xi = \frac{2\tau}{\Theta_f \sqrt{t_c}}$, for reasons discussed in section 2.4.

and a new second front can commence growing at $\xi = -2\beta^* / \Delta$, i. e., at

$$x = x_2 = s(t_2) + \frac{2\delta\mu\beta^*}{\Delta}. \quad (2.58)$$

This is indicated in figure 6 by the curve labelled ‘secondary band’. Note that as τ increases, the secondary band is nucleated ahead of the first front, and then it grows outwards a little to the left but more noticeably to the right. A snapshot of the forming secondary band is shown in figure 7.

In this theory the secondary band carries on growing and there is no further nucleation. The reason for this lies in the assumption that the quadratic approximation in (2.29) remains valid. This in turn was derived from the given function A in (2.9) and the boundary layer description for B in (2.12) and (2.13). While the expression for A remains the same, the boundary layer description for B must be altered when the primary front ceases to move.

We will not attempt this subsequent band formation analysis here, but content ourselves with indicating the form of the characteristic diagram we expect to be appropriate; this is shown in figure 8. Such a diagram for subsidiary bands will be appropriate if there is a local quadratic approximation for C analogous to that in

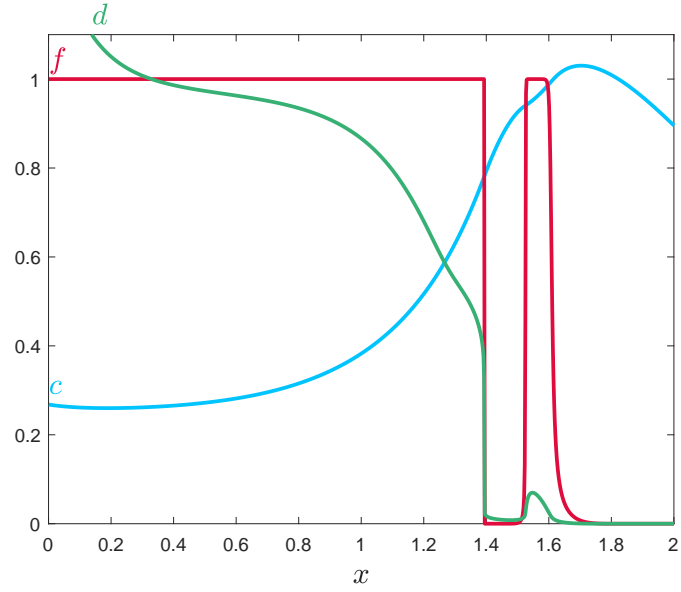


Figure 7: Front propagation at $t = 3.5$. Parameter values as for figure 4. A secondary band has begun to form.

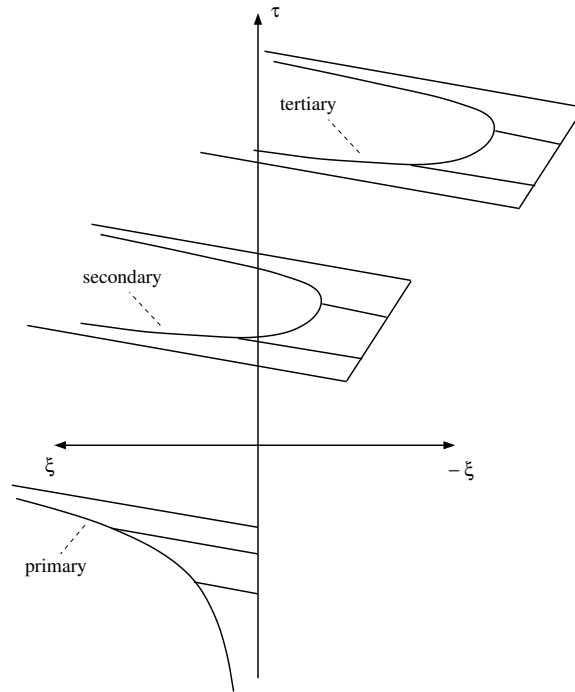


Figure 8: Expected form of the characteristic (τ, ξ) diagram when the boundary layer solution for B is adjusted following subsidiary front formation.

(2.29), with the property that, as τ increases, C first increases and then decreases (unlike (2.29)). We think that the mechanism for this is that when a band front stops, the resulting boundary layer analysis for (2.9) is different to that in (2.12) and (2.13). Further discussion of this is postponed to future work.

3 Numerical results

We solved the problem (2.9) using the method of lines. We discretise $x \in [0, L]$ on a spatial grid of $N + 1$ points (thus the step size is $h = L/(N + 1)$) using second order finite differences, and solve the resulting series of time-dependent ordinary differential equations using `ode15s` in Matlab. For the simulations shown in figures 4, 5 and 7, we used $L = 10$, $N = 4,999$, (thus $h = 0.002$), $\lambda = 5$, $\nu = 0.1$, $\alpha = 0.25$, $\delta = 0.05$, and the computations were terminated at time $t = 10$. Simulation results for $\kappa = 10^{-2}$ at a series of times $t = 0.5, 2.8, 3, 3.5$, were presented in figures 4, 5 and 7.

We wish to track numerically the position of each band. Formally, we define bands as the set of x values for which $f \geq \frac{1}{2}$; a sensible tracking criterion would then be to search numerically for all x such that $f(x) = \frac{1}{2}$ at any value of t . However, once a band has formed and stops evolving spatially, the dynamics of f from (2.9) dictate that the front must sharpen indefinitely so that, regardless of spatial resolution, there will eventually be no grid points in the transition layer as f shifts from one to zero. Therefore, tracking $f(x) = \frac{1}{2}$ is not useful in a practical sense. Instead, we exploit the fact that $\kappa \ll 1$ and apply a filter to the numerical solution at each value of t , which elevates all values $f \geq \frac{1}{2}$ to one and suppresses the remaining values to zero. We then look at the difference between the filtered value of f and the value at the grid point behind it, and we identify the band boundaries as the points where this difference is non-zero. The time when a sharp difference first appears is taken to be the computational band formation time.

3.1 Asymptotic comparison for the primary band

The analysis of the model is based on two small parameters, δ and κ , from which a further two, μ and γ , are derived. Formally these are all small provided $\kappa \ll \delta^2$ but there are practical computational issues to consider. Firstly, κ is related to the necessary time step-size in numerical simulation, and satisfying the constraint $\kappa \ll \delta^2$ can lead to expensive computational times due to increased stiffness. Furthermore, there are boundary layers of $O(\delta)$ and $O(\delta\mu)$ and these need to be numerically resolved which requires $h \leq (\delta\kappa\dot{s})^{1/3}$, where h is the spatial step size in the second order finite difference method. The motivation then in choosing $\delta = 0.1$ arises from the necessity to balance the assumption that $\delta \ll 1$ with the request for reasonable computation times. Comparisons of the simulated and approximate first front positions are shown in figure 9 with the same parameters as in figure 4, as well as $\kappa = 10^{-4}$. Three increasingly accurate approximations are shown, of which the last appears exact, although it is not clear why this should be so.

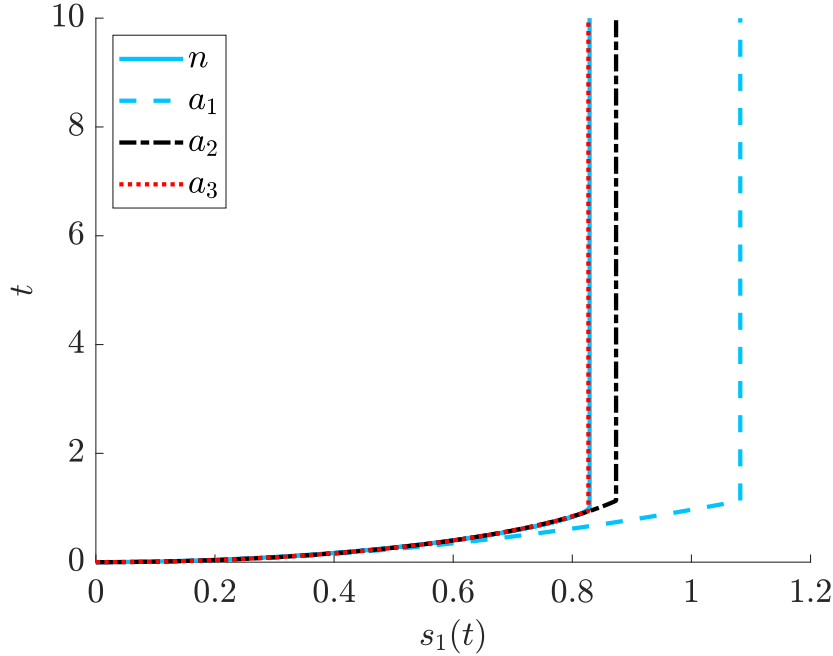


Figure 9: Comparison between simulation (n) and asymptotic analysis (a_1 – a_3) of the evolution and termination of the primary front. The parameter set is $N = 4,999$, $L = 10$, $\lambda = 5$, $\nu = 0.1$, $\alpha = 0.25$, $\delta = 0.1$, and $\kappa = 10^{-4}$; n : numerical solution; a_1 : $s = 2\Theta_f\sqrt{t}$, t_c given by (2.22); a_2 : s given by (2.23), t_c given by (2.22); a_3 : s given by (2.23), $t_c = t_1$ given by (2.55), where for these parameter values, $\gamma = 0.0029$, $\mu = 0.17$, $\beta^* = 2.15$. The last approximation almost overlays the numerical result.

4 Conclusions

The primary purpose of this paper has been to show that a hypothesised transition equation for heterogeneous nucleation can provide a means of eliminating the singularity which is otherwise present in the classic Keller–Rubinow model for Liesegang band formation. This model (the supersaturation model) is one of two which have been principally suggested to explain the phenomenon. The other is the post-nucleation model (Flicker and Ross 1974, Venzl and Ross 1982a,b) in which precipitate nucleation is supposed to occur uniformly in space, with the subsequent bands forming by the process of Ostwald ripening. Models for band formation in this case are commonly of Cahn–Hilliard type (e.g., Falkowitz and Keller 1988). The post-nucleation theory is applicable in experiments with uniform initial conditions, but in the experimental context considered here, where there are strong gradients of the silver ion, the supersaturation theory may be more appropriate.

We find that our modification of the Keller–Rubinow model does indeed provide a resolution of its apparent singularity and ill-posedness, and we have gone some way towards explaining the results which are found numerically. In particular, we are able to predict quantitatively the time and location of the termination of the first band, and also the nucleation of the second band. Subsequent front terminations and band

nucleations require further analysis of the model, and we hope to develop such an analysis in future work.

Data accessibility

The numerical codes used are provided in electronic supplementary material.

Competing interests

We have no competing interests.

Authors' contributions

A. C. F. devised the project, and wrote the paper. J. M. D. and I. R. M. constructed and solved the numerical model. All authors performed the literature review, and contributed to the analytic and numerical work. All authors worked on the final text.

Acknowledgements

We thank Richard Katz of Oxford University, with whose collaboration the original experimental work was done.

Funding statement

This publication has emanated from research conducted with the financial support of Science Foundation Ireland under grant numbers SFI/12/IA/1683 and SFI/13/IA/1923.

Ethics statement

This research poses no ethical considerations.

References

- Aldous, D. J. 1999 Deterministic and stochastic models for coalescence (aggregation and coagulation): a review of the mean-field theory for probabilists. *Bernoulli* **5**, 3–48.
- Avrami, M. 1939 Kinetics of phase change. I. General theory. *J. Chem. Phys.* **7**, 1,103–1,112.
- Becker, R. and W. Döring 1935 Kinetische Behandlung der Keimbildung in übersättigten Dämpfen. *Ann. Phys. (5)* **24**, 719–752.
- Ben-Naim, E. and P. L. Krapivsky 1996 Nucleation and growth in one dimension. *Phys. Rev. E* **54** (4), 3,562–3,568.
- Büki, A., É. Kárpáti-Smidróczki and M. Zrínyi 1995 Computer simulation of regular Liesegang structures. *J. Chem. Phys.* **103**, 10,387–10,392.

- Cahn, J. W. and J. E. Hilliard 1958 Free energy of a non-uniform system. I. Interfacial free energy. *J. Chem. Phys.* **28** (2), 258–267.
- Dowty, E. 1980 Crystal growth and nucleation theory and the numerical simulation of igneous crystallisation. In: *Physics of magmatic processes*, ed. R. B. Hargraves, pp. 419–485. Princeton University Press, Princeton, N. J.
- Duley, J. M., A. C. Fowler, I. R. Moyles and S. B. G. O’Brien 2017 On the Keller–Rubinow model for Liesegang ring formation. *Proc. R. Soc. Lond. A* **473**, 20170128.
- Falkowitz, M. and J. B. Keller 1988 Precipitation pattern formation. *J. Chem. Phys.* **88**, 416–421.
- Feeney, R., S. L. Schmidt, P. Strickholm, J. Chadam and P. Ortoleva 1983 Periodic precipitation and coarsening waves: applications of the competitive particle growth model. *J. Chem. Phys.* **78** (3), 1,293–1,311.
- Fiałkowski, M., A. Bitner and B. A. Grzybowski 2005 Wave optics and Liesegang rings. *Phys. Rev. Letts.* **94**, 018303.
- Flicker, M. and J. Ross 1974 Mechanism of chemical instability for periodic precipitation. *J. Chem. Phys.* **60**, 3,458–3,465.
- Fowler, A. C. 1997 *Mathematical models in the applied sciences*. C. U. P., Cambridge.
- George, J. and G. Varghese 2005 Intermediate colloidal formation and the varying width of periodic precipitation bands in reaction-diffusion systems. *J. Colloid Interf. Sci.* **282**, 397–402.
- Henisch, H. K. 1988 *Crystals in gels and Liesegang rings*. C. U. P., Cambridge.
- Hilhorst, D., R. van der Hout, M. Mimura and I. Ohnishi 2009 A mathematical study of the one-dimensional Keller and Rubinow model for Liesegang bands. *J. Stat. Phys.* **135**, 107–132.
- Jablczynski, K. La formation rythmique des précipités: les anneaux de Liesegang. 1923 *Bull. Soc. Chim. Fr.* (4) **33**, 1,592–1,597.
- Kai, S., S. C. Müller and J. Ross 1982 Measurements of temporal and spatial sequences of events in periodic precipitation processes. *J. Chem. Phys.* **76**, 1,392–1,406.
- Keller, J. B. and S. I. Rubinow 1981 Recurrent precipitation and Liesegang rings. *J. Chem. Phys.* **74**, 5,000–5,007.
- Lagzi, I. 2003 Simulation of Liesegang patterns: effect of reversible complex formation of precipitate. *J. Phys. Chem. B* **107**, 13,750–13,753.

- Lagzi, I. and D. Ueyama 2009 Pattern transition between periodic Liesegang pattern and crystal growth regime in reaction-diffusion systems. *Chem. Phys. Letts.* **468**, 188–192.
- Lexa, D. and D. Holba 1993 Periodic precipitation of silver chromate/dichromate in gelatin. *Colloid Polymer Sci.* **271**, 884–890.
- Liesegang, R. E. 1896 Über einige Eigenschaften von Gallerten. *Naturwiss. Wochenschr.* **11**, 353–362.
- Lifshitz, I. M. and V. V. Slyozov 1961 The kinetics of precipitation from supersaturated solid solutions. *J. Phys. Chem. Solids* **19**, 35–50.
- Morse, H. W. and G. W. Pierce 1903 Diffusion and supersaturation in gelatine. *Phys. Rev. (Ser. 1)* **17**, 129–150.
- Müller, S. C. and J. Ross 2003 Spatial structure formation in precipitation reactions. *J. Phys. Chem. A* **107**, 7,997–8,008.
- Ostwald, W. 1897a Studien über die Bildung und Umwandlung fester Körper. *Zeit. Physik. Chem.* **22**, 289–330.
- Ostwald, W. 1897b A-Linien von R. E. Liesegang. *Zeit. Physik. Chem.* **23**, 365.
- Polezhaev, A. A. and S. C. Müller 1994 Complexity of precipitation patterns: Comparison of simulation with experiment. *Chaos* **4**, 631–636.
- Prager, S. 1956 Periodic precipitation. *J. Chem. Phys.* **25**, 279–283.
- Rácz, Z. 1999 Formation of Liesegang patterns. *Physica A* **274**, 50–59.
- Skorobogatov, G. A. and A. V. Kamenskii 2006 A model for the formation of Liesegang rings under stimulated precipitation conditions. *Russ. J. Phys. Chem.* **80** (5), 714–725.
- Smith, D. 1984 On Ostwald’s supersaturation theory of rhythmic precipitation (Liesegang’s rings). *J. Chem. Phys.* **81**, 3,102–3,115.
- Smoukov, S. K., I. Lagzi and B. A. Grzybowski 2011 Independence of primary and secondary structures in periodic precipitation patterns. *J. Phys. Chem. Lett.* **2**, 345–349.
- Stern, K. H. 1954 The Liesegang phenomenon. *Chem. Revs.* **54**, 79–99.
- Toramaru, A., T. Harada and T. Okamura 2003 Experimental pattern transitions in a Liesegang system. *Physica D* **183**, 133–140.
- Venzl, G. 1986 Pattern formation in precipitation processes. II. A postnucleation theory of Liesegang bands. *J. Chem. Phys.* **85**, 2,006–2,011.

- Venzl, G. and J. Ross 1982a Nucleation and colloidal growth in concentration gradients (Liesegang rings). *J. Chem. Phys.* **77**, 1,302–1,307.
- Venzl, G. and J. Ross 1982b Comments on pattern formation in precipitation processes. *J. Chem. Phys.* **77**, 1,308–1,313.
- Wagner, C. 1950 Mathematical analysis of the formation of periodic precipitations. *J. Colloid Sci.* **5**, 85–97.
- Willgoose, G., R. L. Bras and I. Rodriguez-Iturbe 1991 A coupled channel network growth and hillslope evolution model, 1, theory. *Water Resour. Res.* **27**, 1,671–1,684.
- Zegeling, P. A., I. Lagzi and F. Izsák 2011 Transition of Liesegang precipitation systems: simulations with an adaptive grid PDE method. *Commun. Comput. Phys.* **10**, 867–881.
- Zel’dovich, Y. B., G. I. Barenblatt and R. L. Salganik 1962 Quasiperiodic precipitation upon mutual diffusion of two substances (Liesegang rings). *Dokl. Akad. Nauk SSSR* **140** (6), 1,281–1,284. (In Russian.)